Available online at www.sciencedirect.com
ScienceDirect
Journal of the European Ceramic Society 30 (2010) 2147–2154
www.elsevier.com/locate/jeurceramsoc

Microstructure, mechanical, thermal, and oxidation properties of a $Zr_2[Al(Si)]_4C_5$–SiC composite prepared by in situ reaction/hot-pressing

Ling-Feng He [a,b], Fang-Zhi Li [a,b], Xin-Po Lu [a,b], Yi-Wang Bao [a], Yan-Chun Zhou [a,*]

[a] *Shenyang National Laboratory for Materials Science, Institute of Metal Research, Chinese Academy of Sciences, 72 Wenhua Road, Shenyang 110016, China*
[b] *Graduate School of Chinese Academy of Sciences, Beijing 100039, China*

Available online 1 March 2010

Abstract

The microstructure, mechanical and thermal properties, as well as oxidation behavior, of in situ hot-pressed $Zr_2[Al(Si)]_4C_5$–30 vol.% SiC composite have been characterized. The microstructure is composed of elongated $Zr_2[Al(Si)]_4C_5$ grains and embedded SiC particles. The composite shows superior hardness (Vickers hardness of 16.4 GPa), stiffness (Young's modulus of 386 GPa), strength (bending strength of 353 MPa), and toughness (fracture toughness of 6.62 MPa $m^{1/2}$) compared to a monolithic $Zr_2[Al(Si)]_4C_5$ ceramic. Stiffness is maintained up to 1600 °C (323 GPa) due to clean grain boundaries with no glassy phase. The composite also exhibits higher specific heat capacity and thermal conductivity as well as better oxidation resistance compared to $Zr_2[Al(Si)]_4C_5$.

Keywords: Carbides; Microstructure; Mechanical properties; Thermal properties; Corrosion

1. Introduction

$Zr_2[Al(Si)]_4C_5$ is a new compound formed by adding Al and Si to ZrC; this quaternary carbide shows superior oxidation resistance, strength, specific stiffness and toughness to ZrC.[1–8] Furthermore, the Young's modulus of $Zr_2[Al(Si)]_4C_5$ decreases slowly with increasing temperature and at 1580 °C it remains 81% of that at ambient temperature.[2] However, the hardness of $Zr_2[Al(Si)]_4C_5$ is about half that of ZrC and the fracture toughness is only 3.88 ± 0.16 MPa $m^{1/2}$, which is much lower than other ternary layered carbides, such as Ti_3SiC_2 and Ti_3AlC_2.[9] In addition, as a high-temperature structural material, the oxidation resistance of $Zr_2[Al(Si)]_4C_5$ at high temperature is still unsatisfactory. The oxidation kinetics of $Zr_2[Al(Si)]_4C_5$ generally follows the linear law at 900–1300 °C because no protective Al_2O_3 scale forms on the substrate.[4] Compared to $Zr_2Al_3C_4$,[10] the oxidation resistance of $Zr_2[Al(Si)]_4C_5$ is much better due to the formation of a larger fraction of protective oxidation products, Al_2O_3 and aluminosilicate/mullite ($3Al_2O_3{\cdot}2SiO_2$).[4] In a recent report, an effective approach to improve the high temperature oxidation resistance of $Zr_2Al_3C_4$ by coating a SiC/$ZrSi_2$ layer through silicon pack cementation was developed.[11] It was found that a series of protective oxidation products, such as aluminosilicate glass, mullite and $ZrSiO_4$, retarded the inward diffusion of oxygen during the oxidation of siliconized $Zr_2Al_3C_4$. Thus, one possible way to improve the oxidation resistance of $Zr_2[Al(Si)]_4C_5$ is to incorporate Si-rich compounds.

SiC, which is characterized by its light weight, high hardness and strength, has been widely used as a reinforcing phase to improve the mechanical properties, including hardness, strength, toughness, and wear resistance of ceramics.[12–14] In addition, due to its superior high temperature oxidation resistance, SiC particles or coatings have been commonly used to improve the oxidation resistance of other ceramics, such as ZrB_2, ZrC, and Ti_3SiC_2.[15–17] It is expected that both the mechanical properties and oxidation resistance of $Zr_2[Al(Si)]_4C_5$ can be improved by incorporating SiC particles. Recently, Chen et al.[6] fabricated $Zr_2[Al(Si)]_4C_5$–SiC composites using as-synthesized $Zr_2[Al(Si)]_4C_5$ powders and SiC powders as starting materials. The mechanical properties (flexural strength, fracture toughness and Vickers hardness), thermal properties (thermal conductivity and specific heat capacity) as well as ultrahigh-temperature oxidation resistance of the composites were superior to those of $Zr_2[Al(Si)]_4C_5$.[6,8]

In situ processing, typically consisting of chemical reactions and consolidation in one step, has been widely used for the preparation of ceramic composites. Previous studies[14] on Ti_3SiC_2–SiC composites demonstrated that this method had

* Corresponding author. Tel.: +86 24 23971765; fax: +86 24 23891320.
E-mail address: yczhou@imr.ac.cn (Y.-C. Zhou).

0955-2219/$ – see front matter © 2010 Elsevier Ltd. All rights reserved.
doi:10.1016/j.jeurceramsoc.2010.02.005

many advantages including good microstructural controllability, low contamination, short processing time, decrement in processing temperature and reduction of cost. Therefore, in situ reactive hot-pressing process was adopted in this study to fabricate $Zr_2[Al(Si)]_4C_5$–SiC (denoted as ZASC–SC) composites.

In the present work, the microstructure, mechanical and thermal properties, including hardness, strength, toughness, high-temperature Young's modulus and internal friction, thermal expansion, specific heat capacity, thermal conductivity as well as oxidation resistance of an in situ hot-pressed ZASC–SC composite were studied and compared with those of $Zr_2[Al(Si)]_4C_5$ and SiC. It was found that the ZASC–SC composite showed superior mechanical, thermal properties and oxidation resistance to $Zr_2[Al(Si)]_4C_5$, and a higher toughness than SiC.

2. Experimental procedure

2.1. Material preparation and microstructure characterization

The ZASC–SC composite was fabricated by hot-pressing zirconium (zirconium hydrides), aluminum, silicon, and graphite powders at 1900 °C for 1 h in Ar and then holding at 1600 °C for 0.5 h in low vacuum ($\sim 10^{-2}$ Pa) under a pressure of 30 MPa. The synthesis procedure of the composite was similar to that of $Zr_2[Al(Si)]_4C_5$.[3] The molar ratio of Zr:Al:Si:C for synthesizing ZASC–SC composite was 2:3.6:3.18:7.4, which is an optimized composition to produce two-phase ($Zr_2[Al(Si)]_4C_5$ and SiC) composite without additional impurities. Excess Al and Si powders were added to compensate for their loss during the heating process. Deficient carbon in the starting materials is properly related to intrinsic carbon vacancies in the two carbides.

The density of sintered samples was determined by the Archimedes method. Phase identification was conducted via a step-scanning X-ray diffractometer with Cu Kα radiation (Rigaku D/max–2400, Tokyo, Japan). Microstructure analysis was carried out by a SUPRA 35 scanning electron microscope (SEM) (LEO, Oberkochen, Germany). The samples were etched for 1 h in a 1:1:5 (by volume) solution of HF, HNO_3 and H_2O before SEM observation. A 300 kV Tecnai G^2 F30 high-resolution transmission electron microscope (HRTEM) (FEI, Eindhoven, Netherlands) equipped with an EDS system was used to characterize the microstructure of samples. Thin-foil specimens for TEM observations were prepared by slicing, mechanical grinding to 20 μm, dimpling down to 10 μm, and ion milling at 4.0 kV.

2.2. Mechanical property test

To reveal the temperature dependence of Young's modulus and internal friction of the ZASC–SC composite, a rectangular beam-like sample with dimensions of 3 mm × 15 mm × 40 mm was suspended in the nodes of their first bending vibration mode, and measured in a graphite furnace (HTVP 1750 °C, IMCE, Diepenbeek, Belgium) at a heating rate of 3 °C min^{-1} in vacuum on the order of 10^{-1} Pa. The vibration signal, captured by a laser vibrometer, was analyzed with the resonance frequency and damping analyzer.[18] The Young's modulus was calculated from the flexural resonant frequency, f_f, according to ASTM E 1876–97[19]: $E = 0.9465\left(\frac{mf_f^2}{b}\right)\left(\frac{L^3}{t^3}\right)T_1$, with m, L, b and t, the sample weight, length, width, and thickness, respectively. T_1 is a correction factor, depending on the Poisson's ratio and the thickness/length ratio. The internal friction corresponding to the flexural vibration mode was calculated as $Q^{-1} = k/\pi f_f$, where k is the exponential decay parameter of the amplitude of the flexural vibration component.

The Vickers hardness was measured at a load of 50 N with a dwell time of 15 s. The flexural strength (sample size 3 mm × 4 mm × 36 mm) was measured using a three-point bending method in a universal testing machine. The fracture toughness (sample size 4 mm × 8 mm × 36 mm) was determined using single-edge notched beams (SENB). The notch machined by the electrical discharge method was 4 mm in length and 0.1 mm in width with a notch radius of 0.03 mm. The crosshead speeds in strength and toughness measurements were 0.5 and 0.05 mm min^{-1}, respectively, and five samples were used in both strength and toughness measurements.

2.3. Thermal property measurement

The coefficient of thermal expansion (CTE) was measured using a Setsys–24 thermal mechanical analyzer (TMA) (Setaram, Caluire, France) from 100 to 1200 °C with a heating rate of 2 °C min^{-1} under flowing Ar. The dimension of the sample for CTE measurement was Φ5 mm × 10 mm.

A disk sample (Φ12.7 mm × 1.5 mm) was used to measure the specific heat capacity c_p and thermal conductivity kth. The thermal diffusivity was determined from 200 to 1200 °C by a Flashline™ 5000 thermophysical instrument (Anter, Pittsburgh, PA). Prior to the thermal diffusivity test the sample was sprayed with a thin layer of colloidal graphite approximately 10-μm-thick to ensure complete and uniform absorption of the laser pulse. Three measurements were taken at each temperature (200, 400, 600, 800, 1000, and 1200 °C) and the data was calculated using software (Anter FL5000). Using a multi-sample configuration system, and testing a reference sample (graphite) adjacent to ZASC–SC composite, the heat capacity can be obtained parallel with thermal diffusivity.[20] Then, the thermal diffusivities were converted to thermal conductivities using the heat capacity results and measured density of the ZASC–SC composite.

2.4. Oxidation test

A vertical intermediate frequency induction heating (IFIH) furnace[21] was used to evaluate the ultrahigh-temperature oxidation behavior of the ZASC–SC composite in static air. The sample was placed on cylindrical graphite susceptor and then introduced into the intermediate frequency induction coil. An induced current (~27 kHz) was activated and the samples were rapidly heated to about 1300 °C for 1 min and then at about 200 °C min^{-1} up to the test temperatures by adjusting induced power. A two-color pyrometer was used to measure the surface

temperature of the samples. To confirm the true temperature of the sample, a correction experiment was carried out.[21] The duration time for oxidation was 15 min at 1750 °C. At the end of the process, the current was turned off and the sample was cooled down to room temperature at a rate of approximately 500 °C min^{-1}. For comparison, the same oxidation test was also conducted for $Zr_2[Al(Si)]_4C_5$ ceramic.

3. Results and discussion

3.1. Phase composition and microstructure

Fig. 1 shows the XRD patterns of as-prepared ZASC–SC composite as well as pure $Zr_2[Al(Si)]_4C_5$. All the diffraction peaks correspond to $Zr_2[Al(Si)]_4C_5$, β-SiC and α-SiC (mainly 4H and 2H), indicating that the composite is predominantly composed of $Zr_2[Al(Si)]_4C_5$ and SiC. In addition, the measured density of ZASC–SC composite is 4.10 g cm^{-3}, which is about 99.5% of its theoretical value according to the mixture rule (4.50 and 3.22 g cm^{-3} for $Zr_2[Al(Si)]_4C_5$ and SiC, respectively). Fig. 2 shows the SEM micrograph of the polished and etched surface for the composite. The dark SiC grains are embedded in light $Zr_2[Al(Si)]_4C_5$ matrix and both SiC and $Zr_2[Al(Si)]_4C_5$

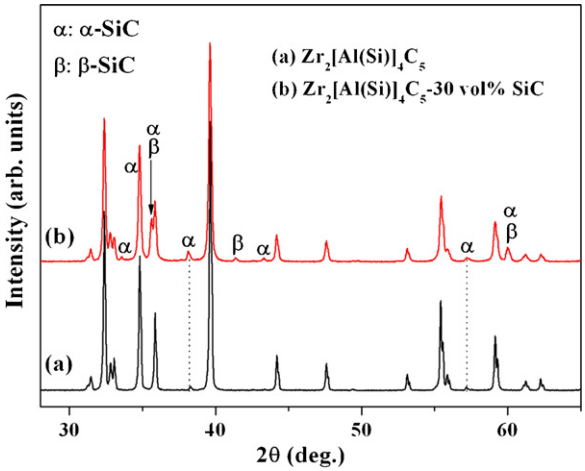

Fig. 1. XRD patterns of as-synthesized $Zr_2[Al(Si)]_4C_5$–30 vol.% SiC composite as well as pure $Zr_2[Al(Si)]_4C_5$ for comparison.

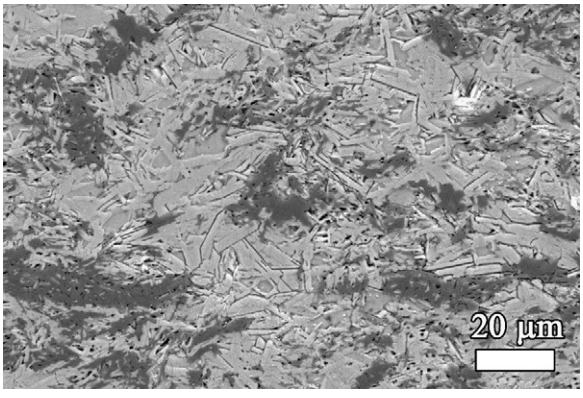

Fig. 2. SEM micrographs of the polished and etched surface of $Zr_2[Al(Si)]_4C_5$–30 vol.% SiC composite.

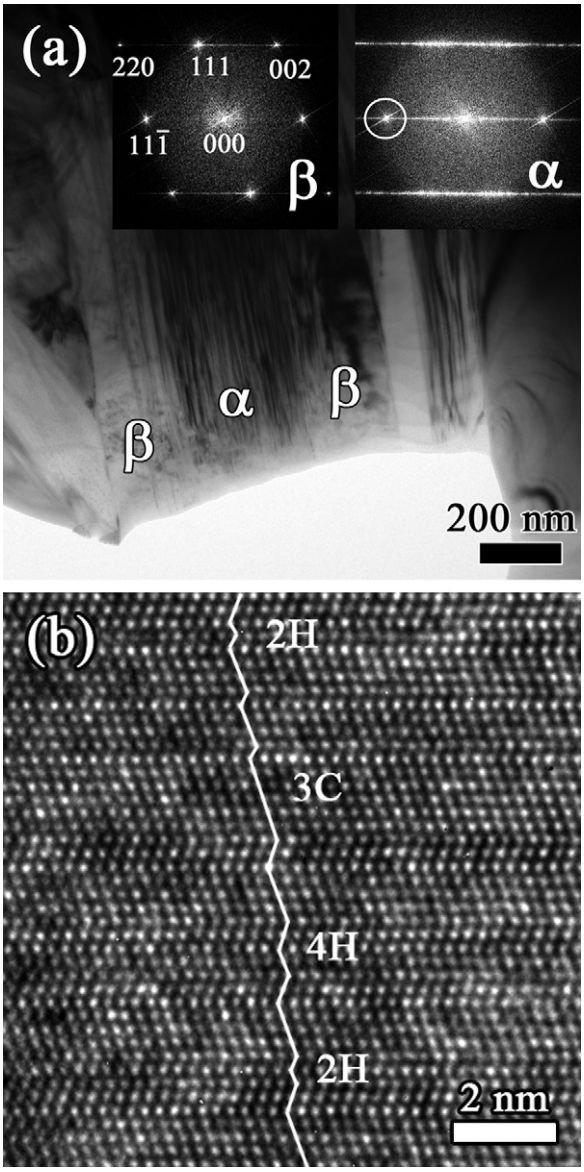

Fig. 3. (a) A representative low-magnification TEM micrograph of SiC grains in the $Zr_2[Al(Si)]_4C_5$–30 vol.% SiC composite. The insets show the FFT image of different zones (α and β) in SiC grain. (b) HRTEM image showing the stacking faults in α zone.

grains mainly show plate-like or elongated morphology. The average grain size of $Zr_2[Al(Si)]_4C_5$ is 5.5 ± 2.7 μm, and the aspect ratio of the elongated grains is about 5.2 ± 2.4. The average grain size of SiC is 1.9 ± 1.2 μm, and the aspect ratio of the elongated grains is about 3.5 ± 1.6.

Fig. 3(a) shows a representative TEM micrograph of a SiC grain in the composite. It exhibits a core (α zone)-envelope (β zone) microstructure, which is quite similar to that of sintered SiC.[22,23] The insets show the FFT image of different zones (α and β) in the SiC grain. The faint streaks in the FFT image of zone α indicate a high density of stacking faults, which is also identified by the HRTEM image (Fig. 3(b)). It can be seen that the lattice stacking sequence is almost random and many SiC polytypes, such as 2H and 4H, exist in proximity to the 3C polymorph. Therefore the bright spot circled in the FFT image

Table 1
Comparison of some properties of $Zr_2[Al(Si)]_4C_5$–30 vol.% SiC composite, $Zr_2[Al(Si)]_4C_5$[3] and SiC[28,29].

Properties	$Zr_2[Al(Si)]_4C_5$–30 vol.% SiC	$Zr_2[Al(Si)]_4C_5$	SiC
Theoretical density ($g\,cm^{-3}$)	4.12	4.50	3.22
Measured density ($g\,cm^{-3}$)	4.01	4.44	3.17
Young's modulus (GPa)	386	361	402
Specific stiffness ($GPa\,cm^3\,g^{-1}$)	96.3	81.3	127
Shear modulus (GPa)	163	153	170
Poisson's ratio	0.18	0.18	0.18
Bulk modulus (GPa)	204	188	210
Hardness (GPa)	16.4	11.7	20–30
Bending strength (MPa)	353 ± 19	302 ± 10	200–600
Fracture toughness ($MPa\,m^{1/2}$)	6.62 ± 0.19	3.88 ± 0.16	2–5
Coefficient of thermal expansion ($\times 10^{-6}\,K^{-1}$)	7.2	8.1	5.1
Specific heat capacity ($J\,kg^{-1}\,K^{-1}$)	584	567	620–770
Thermal conductivity($W\,m^{-1}\,K^{-1}$)	25.3	12.0	80–340

of zone α should correspond to 2H (0 0 2), 3C (1 1 1), 4H (0 0 4), etc.[22] In contrast, the FFT image of zone β shows the feature of β-SiC (3C) and no obvious streaks can be seen, indicating that β zone is almost pure β-SiC.

During the in situ synthesis of ZASC–SC composite, α-SiC (2H, 4H, etc.) and β-SiC (3C) were present, while in the case of in situ synthesis of $Ti_3Si(Al)C_2$–SiC composite, only β-SiC was observed. The main difference between the processing of the two composites lies in the temperature. The sintering temperature of ZASC–SC composite is 1900 °C, which is 300–400 °C higher than that of $Ti_3Si(Al)C_2$–SiC composite. Previous work showed that the 3C to 4H transformation typically started at above 1800 °C in the presence of additions of Al; Al and B; Al, B, and C.[24–26] In the present work, high Al content and high sintering temperature are advantageous to the β → α transformation of SiC. In addition, the transformation occurred with the preferential growth of low-energy coherent β/α interfaces, thus producing α (core)/β (envelope) composite grains.[25]

Fig. 4 is a typical HRTEM image showing the grain boundaries and a triple junction between different $Zr_2[Al(Si)]_4C_5$ grains. The grain boundaries and triple junctions are free of amorphous phase, which is similar to those of $Zr_2[Al(Si)]_4C_5$[2] and (B + C)-doped SiC.[27] The clean grain boundary in ZASC–SC composite lies in the fact that no sintering additive was used when using elemental powders as starting materials; moreover, carbon acts as a reducing agent for oxides at high temperature.

3.2. Mechanical properties

The measured room-temperature mechanical properties of as-synthesized ZASC–SC composite are listed in Table 1. The data are compared to those of $Zr_2[Al(Si)]_4C_5$ and SiC. The room-temperature stiffness of ZASC–SC composite is improved with respect to that of $Zr_2[Al(Si)]_4C_5$, e.g., the Young's modulus of the composite (386 GPa) is about 7% higher than that of $Zr_2[Al(Si)]_4C_5$ (361 GPa). In addition, the specific stiffness of the composite ($96.3\,GPa\,cm^3\,g^{-1}$), i.e., the ratio of Young's modulus to density, is about 12% higher than that of $Zr_2[Al(Si)]_4C_5$ ($81.3\,GPa\,cm^3\,g^{-1}$). The Vickers hardness of the composite is 16.4 GPa, which is 40% higher than that of $Zr_2[Al(Si)]_4C_5$ (11.7 GPa). The flexural strength of the composite (353 ± 19 MPa) is higher than that of $Zr_2[Al(Si)]_4C_5$ (302 ± 10 MPa). ZASC–SC composite exhibits much higher fracture toughness ($6.62 \pm 0.19\,MPa\,m^{1/2}$), which is about 71% higher than that of $Zr_2[Al(Si)]_4C_5$ ($3.88 \pm 0.16\,MPa\,m^{1/2}$). Furthermore, the fracture toughness of the composite is comparable to the damage-tolerant layered carbides, MAX phases, such as Ti_3SiC_2 and Ti_3AlC_2.[9] The fracture surface of $Zr_2[Al(Si)]_4C_5$ –30 vol.% SiC composite shown in Fig. 5(a) delineates a rough surface morphology with many jagged fractured and fragmentized grains. In addition, the crack path (Fig. 5(b)) shows that the cracks propagate relatively straight in the $Zr_2[Al(Si)]_4C_5$ matrix, while the cracks deflect markedly around the SiC particles.

The hardness and stiffness of ZASC–SC composite should have close relation to the properties of $Zr_2[Al(Si)]_4C_5$ and SiC. SiC has a high hardness (20–30 GPa) and stiffness (Young's modulus of 403 GPa), which results in a higher hardness and

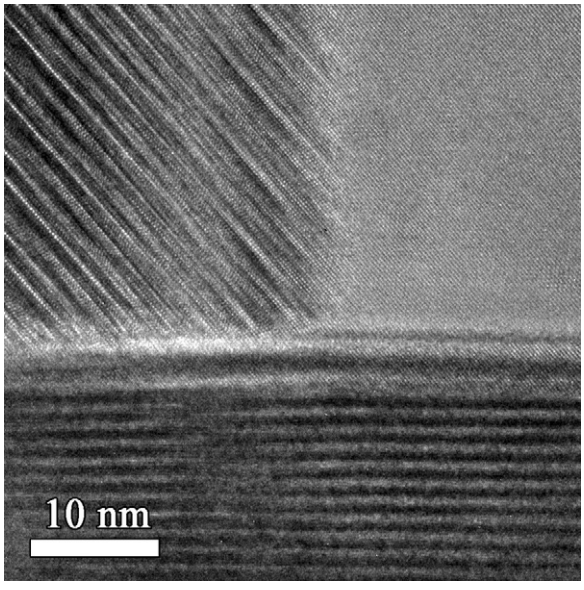

Fig. 4. A typical HRTEM image of a triple junction of $Zr_2[Al(Si)]_4C_5$ grains in $Zr_2[Al(Si)]_4C_5$–30 vol.% SiC composite.

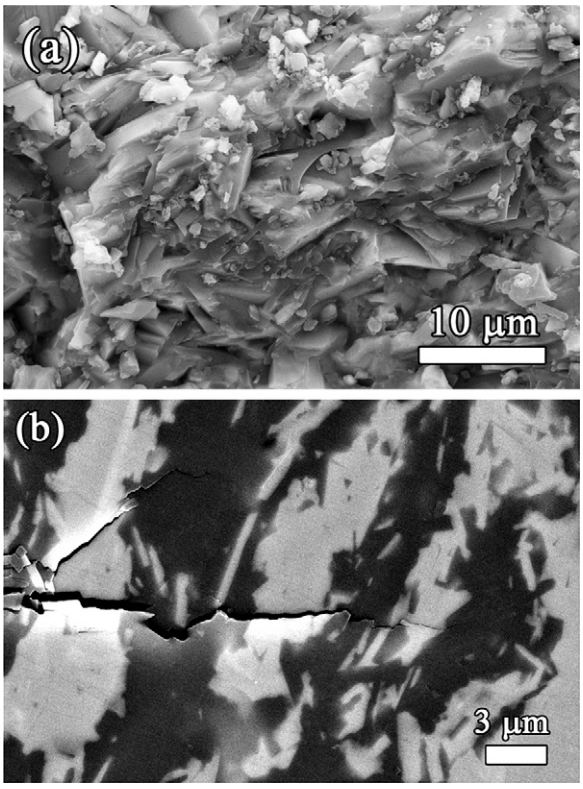

Fig. 5. SEM micrograph of (a) the fracture surface of $Zr_2[Al(Si)]_4C_5$–30 vol.% SiC composite and (b) crack propagation path from Vickers indentation in the composite.

stiffness for the composite compared to $Zr_2[Al(Si)]_4C_5$. Furthermore, the specific stiffness of the composite is greatly enhanced by adding the lower density SiC particles into $Zr_2[Al(Si)]_4C_5$ matrix. The fracture toughness of $Zr_2[Al(Si)]_4C_5$ is significantly improved by incorporating SiC particles. The high fracture toughness is ascribed to the high energy dissipation during fracture, which should be associated with residual stresses in the composite. The mismatch in the coefficients of thermal expansion and elastic moduli between $Zr_2[Al(Si)]_4C_5$ matrix and the SiC particles results in the generation of residual stresses in the particles and surrounding matrix for cooling after sintering. The radial matrix stress (σ_{mr}) and the tangential matrix stress ($\sigma_{m\theta} = -\sigma_{mr}/2$) can be calculated according to the following equation:[30]

$$\sigma_{mr} = \frac{(\alpha_p - \alpha_m)\Delta T}{[(1+\nu_m)/2E_m] + [(1-2\nu_p)/E_p]} \quad (1)$$

where the subscripts p and m refer to the particle and matrix, respectively, ν is the Poisson's ratio, and ΔT is the temperature range over which stresses are not relieved by a diffusive process (assuming 1000 °C). Using the data in Table 1, matrix stresses are calculated as $\sigma_{mr} = -930$ MPa (compressive) and $\sigma_{m\theta} = 465$ MPa (tensile). Therefore, the cracks propagate readily in the $Zr_2[Al(Si)]_4C_5$ matrix due to the tensile tangential stress. On the contrary, due to the stress equilibrium in the matrix and particles, the tangential particle stress is compressive, which inhibits crack propagation. This is the fundamental reason for the relatively direct cracks in the $Zr_2[Al(Si)]_4C_5$ matrix while the

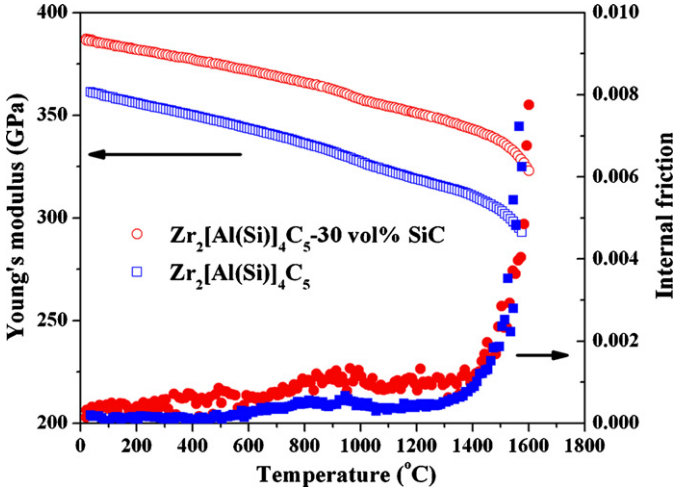

Fig. 6. Temperature dependence of Young's modulus and internal friction for $Zr_2[Al(Si)]_4C_5$–30 vol.% SiC composite as well as $Zr_2[Al(Si)]_4C_5$ for comparison.

cracks are deflected around the SiC particles, and the inhibition of crack propagation through the SiC particles is predominantly responsible for the high fracture toughness. The ZASC–SC composite has a superior fracture toughness and smaller grain size compared with $Zr_2[Al(Si)]_4C_5$, therefore the composite should have a much higher strength than the matrix according to the following equation derived from classic fracture mechanics[31]:

$$\sigma = \frac{\sqrt{2}}{\sqrt{\pi}} \frac{K_{1C}}{\sqrt{D}} \quad (2)$$

where σ is the tensile stress, K_{1C} is the fracture toughness, D is the grain size. However, the strength of the composite is only slightly higher than that of $Zr_2[Al(Si)]_4C_5$. Generally speaking, the tensile tangential stress in the matrix will result in a relatively low strength. In the case of $Ti_3Si(Al)C_2$–SiC composite, increasing SiC content can improve the stiffness and hardness while decreasing the strength.[14]

Fig. 6 shows the temperature dependence of Young's modulus and internal friction of the ZASC–SC composite, as well as $Zr_2[Al(Si)]_4C_5$ for comparison. The Young's modulus of the composite decreases slowly and almost linearly with increasing temperature up to about 1450 °C. After that, it decreases at a much faster rate. Meanwhile, the internal friction increases sharply. During the heating and cooling process, no relaxation peak was observed, however a high temperature damping background was present. This result is similar to the mechanical spectroscopy of $Zr_2[Al(Si)]_4C_5$ and (B + C)-doped SiC[27]. Due to the clean grain boundary and tightly interlocked grains at grain-edge triple junctions, the relaxation resulting from grain-boundary sliding at high temperature was suppressed and the internal friction curve simply experienced an exponential-like increase. It is conceivable to expect a low viscoelastic response and high macroscopic deformation resistance at elevated temperatures for the ZASC–SC composite. The remaining Young's modulus of the ZASC–SC composite at 1600 °C (323 GPa), which is much higher than those of $Zr_2[Al(Si)]_4C_5$ and most refractory compounds,[32,33] rendering the ZASC–SC

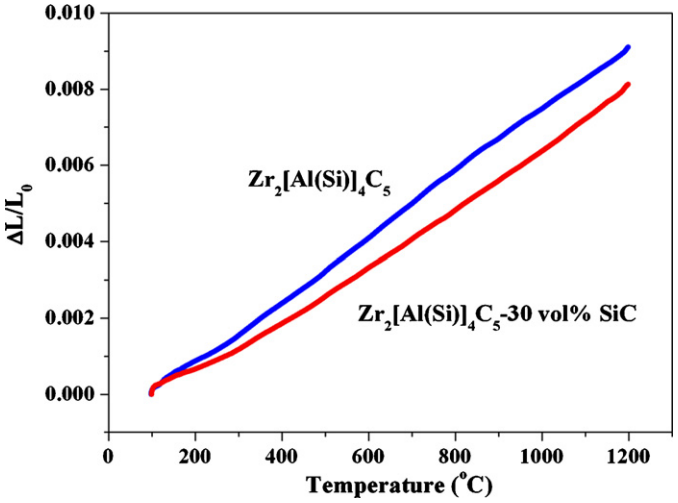

Fig. 7. Thermal expansions of $Zr_2[Al(Si)]_4C_5$–30 vol.% SiC composite during heating at a rate of 2 °C min^{-1} as well as $Zr_2[Al(Si)]_4C_5$ for comparison.

composite as a potential high-temperature structural material.

3.3. Thermal properties

Fig. 7 shows the thermal expansion behavior of the ZASC–SC composite in the temperature range of 100–1200 °C. For comparison, the thermal expansion curve of $Zr_2[Al(Si)]_4C_5$ is also given. A least-squares fit of the data yields the coefficient of thermal expansion (CTE) of $7.2 \times 10^{-6}\,K^{-1}$, which is lower than that of $Zr_2[Al(Si)]_4C_5$ ($8.1 \times 10^{-6}\,K^{-1}$). The average CTE of the ZASC–SC composite can be simply calculated according to the Turner equation[34]:

$$\alpha_c = \frac{\sum_i \alpha_i B_i V_i}{\sum B_i V_i} \quad (3)$$

where α_i, B_i, and V_i are the CTE, bulk modulus, and volume fraction, respectively. These parameters for $Zr_2[Al(Si)]_4C_5$ and SiC are listed in Table 1. Assuming that the V and B for $Zr_2[Al(Si)]_4C_5$ and SiC are independent of temperature, the average CTE for the composite is calculated to be $6.6 \times 10^{-6}\,K^{-1}$, which is lower than the measured data of the composite ($7.2 \times 10^{-6}\,K^{-1}$), indicating that the CTE of $Zr_2[Al(Si)]_4C_5$ in only partially resisted by the SiC particles.

The temperature dependence of specific heat capacity of ZASC–SC is plotted in Fig. 8(a). For comparison, that of $Zr_2[Al(Si)]_4C_5$[3] is also given. Curve fitting of the experimental data yields:

$$c_P = 938 + 75.0 \times 10^{-3} T - 339 \times 10^5 T^{-2} \quad (4)$$

with R^2 of 0.97. The specific heat capacities of ZASC–SC at 300 and 1600 K are extrapolated to be 584 and 1045 J kg^{-1} K^{-1}, respectively. The specific heat capacity of ZASC–SC is much higher than that of $Zr_2[Al(Si)]_4C_5$.

The thermal conductivity, k_{total}, of ZASC–SC is plotted in Fig. 8(b). For comparison, the thermal conductivity of $Zr_2[Al(Si)]_4C_5$ is also given.[3] A least-squares fit of the data

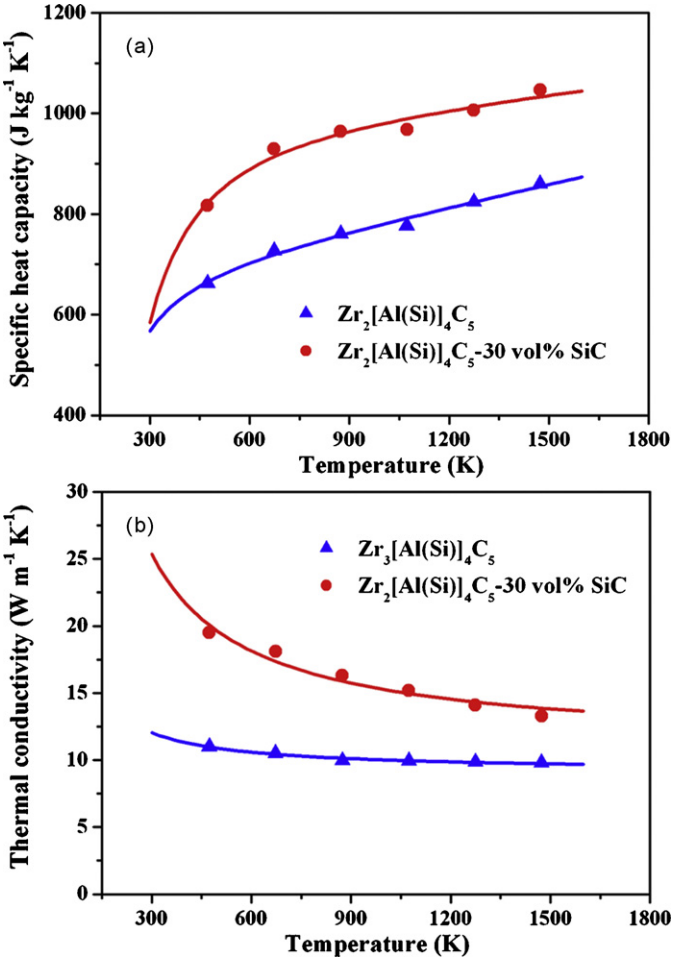

Fig. 8. Temperature dependence of (a) specific heat capacity and (b) thermal conductivity of $Zr_2[Al(Si)]_4C_5$–30 vol.% SiC composite and $Zr_2[Al(Si)]_4C_5$ ceramic.

yields the following relationship:

$$k_{total} = \frac{10.94 + 4319.5}{T} \quad (5)$$

with an R^2 of 0.95. The thermal conductivities of ZASC–SC at 300 and 1600 K are extrapolated to be 25.3 and 13.6 W m^{-1} K^{-1}, respectively. Compared with $Zr_2[Al(Si)]_4C_5$, the ZASC–SC composite has a much improved thermal conductivity over the entire temperature range.

3.4. Oxidation resistance

Fig. 9 shows the cross-sectional and surface morphologies of $Zr_2[Al(Si)]_4C_5$ and the ZASC–SC composite exposed in static air at 1750 °C for 15 min. The corresponding composition of the oxide scales for the two samples is shown in Fig. 10. The average oxide scale thickness of $Zr_2[Al(Si)]_4C_5$ and ZASC–SC composite is about 120 (Fig. 9(a)) and 70 μm (Fig. 9(b)), respectively, indicating that the ZASC–SC composite shows better oxidation resistance. The surface of $Zr_2[Al(Si)]_4C_5$ is heavily cracked and rough (Fig. 9(c)), while that of the composite is relatively smooth (Fig. 9(d)). In addition, a high-magnification surface morphology image of $Zr_2[Al(Si)]_4C_5$ (Fig. 9(e)) shows

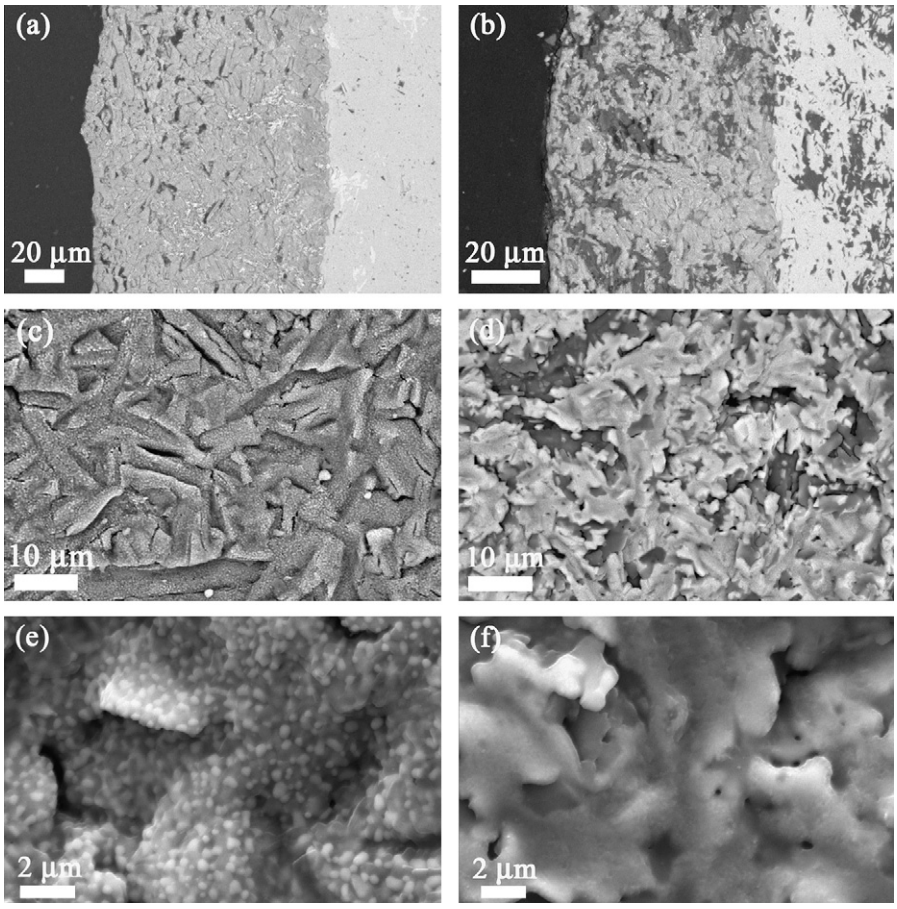

Fig. 9. Cross-sectional and surface morphologies of $Zr_2[Al(Si)]_4C_5$ ((a), (c) and (e)) and $Zr_2[Al(Si)]_4C_5$–30 vol.% SiC composite ((b), (d) and (f)) exposed in static air at 1750 °C for 15 min.

the presence of white ZrO_2 grains (100–300 nm in size) embedded in a darker matrix, which is mainly composed of Al_2O_3 (Fig. 10(a)). For the ZASC–SC composite, a high-magnification SEM image from the lighter contrast region of Fig. 9(e) is relatively featureless (Fig. 9(f)), implying that ZrO_2 grain growth was inhibited during oxidation of the composite with respect to $Zr_2[Al(Si)]_4C_5$. Based on the XRD results, there appears to be a considerable amount of t-ZrO_2 remaining in the oxide scales of the composite (Fig. 10(b)), which is a good evidence for the existence of nanocrystalline ZrO_2 grains. Due to a lack of a stabilizing agent for ZrO_2, t-ZrO_2 should transform to m-ZrO_2 upon cooling to room temperature. However, small ZrO_2 grains (especially below 10 nm) display a high activation energy barrier for the martensitic t → m transformation, resulting in the coexistence of both t- and m-ZrO_2 phases.[35,36] The metastable t-ZrO_2 would be expected to gradually transform into m-ZrO_2 as the grains grow. The enhancement of oxidation resistance of the composite with respect to $Zr_2[Al(Si)]_4C_5$ can be ascribed to the formation of Si-containing oxides, such as aluminosilicate glass and mullite, in which the oxygen diffusive rate is very low.[37] In addition, the aluminosilicate glass can fill up pores and cracks during oxidation,[11,38] leading to the inhibition of further oxidation. This can be confirmed by the relatively smooth surface of the ZASC–SC composite after oxidation.

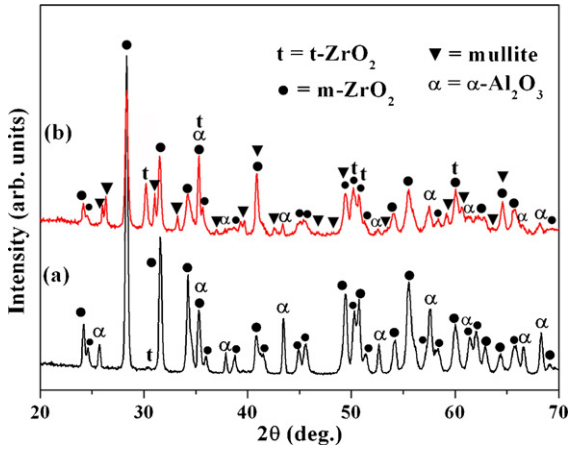

Fig. 10. XRD patterns of (a) $Zr_2[Al(Si)]_4C_5$ and (b) $Zr_2[Al(Si)]_4C_5$–30 vol.% SiC composite oxidized at 1750 °C for 15 min.

4. Conclusions

A $Zr_2[Al(Si)]_4C_5$–30 vol.% SiC composite was fabricated by a reactive hot-pressing method using Zr, Al, Si, and graphite as starting materials. The microstructure of the as-synthesized composite is composed of SiC grains embedded in plate-like or elongated $Zr_2[Al(Si)]_4C_5$ matrix. The mechanical and

thermal properties of the composite are superior to those of $Zr_2[Al(Si)]_4C_5$. The composite shows superior hardness (Vickers hardness of 16.4 GPa), stiffness (Young's modulus of 386 GPa), strength (bending strength of 353 MPa), toughness (fracture toughness of 6.62 MPa $m^{1/2}$) compared to a $Zr_2[Al(Si)]_4C_5$ ceramic. The stiffness maintained up to 1600 °C due to its clean grain boundaries, which renders it a good candidate material for high temperature and ultrahigh-temperature applications. In addition, the composite exhibits higher specific heat capacity and thermal conductivity in the measured temperature range as well as ultrahigh-temperature oxidation resistance compared to $Zr_2[Al(Si)]_4C_5$.

Acknowledgements

The authors would like to thank Prof. Greg E. Hilmas in Missouri University of Science and Technology for prereviewing the manuscript and help in correcting English. This work was supported by the National Outstanding Young Scientist Foundation (No. 59925208 for Y. C. Zhou), Natural Science Foundation of China under Grant Nos. 90403027, 50832008 and the "Hundred-Talent Plan" program of the Chinese Academy of Sciences.

References

1. Fukuda K, Hisamura M, Iwata T, Tera N, Sato K. Synthesis, crystal structure, and thermoelectric properties of a new carbide $Zr_2[Al_{3.56}Si_{0.44}]C_5$. *J Solid State Chem* 2007;**180**:1809–15.
2. Lin ZJ, He LF, Wang JY, Li MS, Bao YW, Zhou YC. Atomic-scale microstructures and elastic properties of quaternary Zr–Al–Si–C ceramics. *Acta Mater* 2008;**56**:2022–31.
3. He LF, Bao YW, Wang JY, Li MS, Zhou YC. Mechanical and thermophysical properties of Zr–Al–Si–C ceramics. *J Am Ceram Soc* 2009;**92**:445–51.
4. He LF, Bao YW, Li MS, Wang JY, Zhou YC. Oxidation of $Zr_2[Al(Si)]_4C_5$ and $Zr_3[Al(Si)]_4C_6$ in air. *J Mater Res* 2008;**23**:3339–46.
5. He LF, Lu XP, Bao YW, Wang JY, Zhou YC. High temperature internal friction, stiffness, and strength of Zr–Al(Si)–C ceramics. *Scr Mater* 2009;**61**:60–3.
6. Chen G, Zhang R, Zhang X, Han W. Microstructure and properties of hot pressed $Zr_2(Al(Si))_4C_5$/SiC composites. *J Alloys Compd* 2009;**481**:877–80.
7. Chen G, Zhang R, Zhang X, Zhao L, Han W. Oxidation-induced crack healing in $Zr_2Al_4C_5$ ceramic. *Mater Des* 2009;**30**:3602–7.
8. Chen G, Zhang R, Zhang X, Hu P, Han W. Oxidation resistance of $Zr_2[Al(Si)]_4C_5$ based composites at ultra-high-temperature. *Scr Mater* 2009;**61**:697–700.
9. Wan DT, Meng FL, Zhou YC, Bao YW, Chen JX. Effect of grain size, notch width, and testing temperature on the fracture toughness of $Ti_3Si(Al)C_2$ and Ti_3AlC_2 using the chevron-notched beam (CNB) method. *J Eur Ceram Soc* 2008;**28**:663–9.
10. He LF, Lin ZJ, Bao YW, Li MS, Wang JY, Zhou YC. Isothermal oxidation of bulk $Zr_2Al_3C_4$ at 500 to 1000 °C in air. *J Mater Res* 2008;**23**:359–66.
11. He LF, Bao YW, Li MS, Wang JY, Zhou YC. Improving the high-temperature oxidation resistance of $Zr_2Al_3C_4$ by silicon pack cementation. *J Mater Res* 2008;**23**:2275–82.
12. Bhattacharya AK, Petrovic JJ. Hardness and fracture toughness of SiC-particle-reinforced $MoSi_2$ composites. *J Am Ceram Soc* 1991;**90**: 2700–3.
13. Chamberlain AL, Fahrenholtz WG, Hilmas GE, Ellerby DT. High-strength zirconium diboride-based ceramics. *J Am Ceram Soc* 2004;**87**:1170–2.
14. Wan DT, Zhou YC, Bao YW, Yan CK. In situ reaction synthesis and characterization of $Ti_3Si(Al)C_2$/SiC composites. *Ceram Int* 2006;**32**:883–90.
15. Opeka MM, Talmy IG, Wuchina EJ, Zaykoski JA, Causey SJ. Mechanical, thermal, and oxidation properties of refractory hafnium and zirconium compounds. *J Eur Ceram Soc* 1999;**19**:2405–14.
16. Opeka MM, Talmy IG, Zaykoski JA. Oxidation-based materials selection for 2000 °C + hypersonic aerosurfaces: theoretical considerations and historical experience. *J Mater Sci* 2004;**39**:5887–904.
17. Zhou YC, Wan DT, Bao YW, Wang JY. In situ processing and high-temperature properties of $Ti_3Si(Al)C_2$/SiC composites. *Int J Appl Ceram Technol* 2006;**3**:47–54.
18. Roebben G, Bollen B, Brebels A, Van Humbeeck J, Van der Biest O. Impulse excitation apparatus to measure resonant frequencies, elastic moduli, and internal friction at room and high temperature. *Rev Sci Intrum* 1997;**68**:4511–5.
19. ASTM E 1876–1897. *Standard test method for dynamic Young's modulus, shear modulus, and Poisson's ratio by impulse excitation of vibration*. West Conshohocken, PA: American Society for Testing Materials; 1998.
20. Gaal PS, Thermitus MA, Stroe DE. Thermal conductivity measurements using the flash method. *J Therm Anal Calorim* 2004;**78**:185–9.
21. He LF, Zhong HB, Xu JJ, Li MS, Bao YW, Wang JY, Zhou YC. Ultrahigh temperature oxidation of $Zr_2Al_3C_4$ via rapid induction heating. *Scr Mater* 2009;**60**:547–50.
22. Heuer AH, Fryburg GA, Ogbuji LU, Mitchell TE, Shinozaki S. $\beta \rightarrow \alpha$ transformation in polycrystalline SiC. I. Microstructural aspects. *J Am Ceram Soc* 1978;**61**:406–12.
23. Ogbuji LU, Mitchell TE, Heuer AH, Shinozaki S. The $\beta \rightarrow \alpha$ transformation in polycrystalline SiC. IV. A comparison of conventionally sintered, hot-pressed, reaction-sintered, and chemically vapor-deposited samples. *J Am Ceram Soc* 1981;**64**:100–5.
24. Zhang XF, Yang Q, De Jonghe LC. Microstructure development in hot-pressed silicon carbide: effects of aluminum, boron, and carbon additives. *Acta Mater* 2003;**51**:3849–60.
25. Zhan GD, Ikuhara Y, Mitomo M, Xie RJ, Sakuma T, Mukherjee AK. Microstructural analysis of liquid-phase-sintered β-silicon carbide. *J Am Ceram Soc* 2002;**85**:430–6.
26. Hilmas GE, Tien TY. Effect of AlN and Al_2O_3 additions on the phase relationships and morphology of SiC. Part II. Microstructural observations. *J Mater Sci* 1999;**34**:5613–21.
27. Pezzotti G, Kleebe HJ, Ota K. Grain-boundary viscosity of polycrystalline silicon carbides. *J Am Ceram Soc* 1998;**81**:3293–9.
28. Green DJ. *An introduction to the mechanical properties of ceramics*. Cambridge: Cambridge University Press; 1998.
29. Snead LL, Nozawa T, Katoh Y, Byun TS, Kondo S, Petti DA. Handbook of SiC properties for fuel performance modeling. *J Nucl Mater* 2007;**371**:329–77.
30. Wei GC, Becher PF. Improvements in mechanical properties in SiC by the addition of TiC particles. *J Am Ceram Soc* 1984;**67**:571–4.
31. Meyers MA, Chawla KK. *Mechanical behavior of materials*. Cambridge: Cambridge University Press; 2009. p. 408.
32. Rouxel T, Sanglebœuf J, Huger M, Gault C, Besson J, Testu S. Temperature dependence of Young's modulus in Si_3N_4-based ceramics: roles of sintering additives and of SiC-particle content. *Acta Mater* 2002;**50**:1669–82.
33. Wachtman Jr JB, Lam Jr DG. Young's modulus of various refractory materials as a function of temperature. *J Am Ceram Soc* 1959;**42**:254–60.
34. Turner PS. Thermal expansion stressed in reinforced plastics. *J Res NBS* 1946;**37**:239–50.
35. Yoshimura M. Phase stability of zirconia. *Am Ceram Soc Bull* 1988;**67**:1950–5.
36. He LF, Bao YW, Zhou YC. Zirconium aluminum carbides: new precursors for synthesizing ZrO_2–Al_2O_3 composites. *J Am Ceram Soc* 2009;**92**:2751–8.
37. Schneider H, Schreuer J, Hildmann B. Structure and properties of mullite—a review. *J Eur Ceram Soc* 2008;**28**:329–44.
38. Huang XX, Wen GW, Cheng XM, Zhang BY. Oxidation behavior of Al_4SiC_4 ceramic up to 1700 °C. *Corros Sci* 2007;**49**:2059–70.